

Coherent charge oscillations in a bilayer graphene double quantum dot

Received: 14 March 2023

Accepted: 13 November 2023

Published online: 30 November 2023

K. Hecker^{1,2,5}✉, L. Banszerus^{1,2,5}, A. Schäpers¹, S. Möller^{1,2}, A. Peters¹, E. Icking^{1,2}, K. Watanabe³, T. Taniguchi⁴, C. Volk^{1,2} & C. Stampfer^{1,2}

The coherent dynamics of a quantum mechanical two-level system passing through an anti-crossing of two energy levels can give rise to Landau-Zener-Stückelberg-Majorana (LZSM) interference. LZSM interference spectroscopy has proven to be a fruitful tool to investigate charge noise and charge decoherence in semiconductor quantum dots (QDs). Recently, bilayer graphene has developed as a promising platform to host highly tunable QDs potentially useful for hosting spin and valley qubits. So far, in this system no coherent oscillations have been observed and little is known about charge noise in this material. Here, we report coherent charge oscillations and T_2^* charge decoherence times in a bilayer graphene double QD. The charge decoherence times are measured independently using LZSM interference and photon assisted tunneling. Both techniques yield T_2^* average values in the range of 400–500 ps. The observation of charge coherence allows to study the origin and spectral distribution of charge noise in future experiments.

The concept of Landau-Zener-Stückelberg-Majorana (LZSM) interference was first introduced to describe atomic collisions^{1–5} and has found renewed interest with the advent of artificially designed quantum mechanical two-level systems (TLSs) in a variety of solid-state platforms^{6–17}. In particular, LZSM interferometry has been developed into a major work horse to study quantum interference effects in silicon nanowires⁶, nitrogen-vacancy centers in diamond^{7,8}, superconducting qubits⁹ and semiconductor quantum dots (QDs), where it allows to coherently control the electron spin^{10,11} or the spatial position of an electron in a double quantum dot (DQD)^{12–16}. Charge noise limits the charge decoherence time and, e.g., mediated via spin-orbit interaction, the spin decoherence time. Semiconductor QDs have been studied in a wide range of materials, including silicon^{18–20}, germanium²¹ and GaAs^{22,23}. More recently, 2D materials, such as bilayer graphene (BLG) and transition metal dichalcogenides have emerged as potentially interesting alternative materials with appealing properties for highly controllable QDs, interesting for hosting spin and valley qubits²⁴. BLG offers a gate voltage-tunable band gap^{25–27}, small spin-orbit interaction and weak hyperfine coupling²⁴. Important

achievements in BLG QD research include the implementation of charge detection^{28,29}, an understanding of spin-valley coupling^{30–32}, and the measurement of the spin relaxation rate^{33,34}. In addition, QDs have also been realized in WSe₂ and MoS₂ monolayers^{35,36}, which are of interest due to their substantial intrinsic spin-orbit coupling and potential for light-matter coupling. However, despite these recent experimental advances, no coherent oscillations of either charge, spin or valley states have yet been reported in quantum devices based on 2D materials. A priori, it is not obvious that charge coherence can be observed in van der Waals heterostructures such as BLG encapsulated between hexagonal boron nitride (hBN) crystals. In contrast to QDs in semiconductor heterostructures based on GaAs^{37,38} and SiGe^{20,39}, which are buried tens of nm below the dielectric interface, the electron wave function of a BLG QD extends into the hBN making it susceptible to charge noise present due to disorder at the BLG/hBN interface and to impurities in the hBN. So far, no light has been shed on the role of charge noise in graphene QDs.

Here, we demonstrate coherent charge oscillations in a BLG DQD. In contrast to spin, the charge degree of freedom offers faster

¹JARA-FIT and 2nd Institute of Physics, RWTH Aachen University, 52074 Aachen, Germany. ²Peter Grünberg Institute (PGI-9), Forschungszentrum Jülich, 52425 Jülich, Germany. ³Research Center for Functional Materials, National Institute for Materials Science, 1-1 Namiki, Tsukuba 305-0044, Japan. ⁴International Center for Materials Nanoarchitectonics, National Institute for Materials Science, 1-1 Namiki, Tsukuba 305-0044, Japan. ⁵These authors contributed equally: K. Hecker, L. Banszerus. ✉ e-mail: Katrin.Hecker@rwth-aachen.de

dynamics that can be controlled all-electrically using gate electrodes^{40,41}. We operate the DQD in the few electron regime and tune its interdot tunnel coupling to the low GHz regime, which we verify by photon assisted tunneling (PAT) spectroscopy. In a pulsed-gate experiment, we observe LZSM interference oscillations of an excess electron, a characteristic signature of quantum phase coherence. From the PAT experiments, we determine an average ensemble decoherence time T_2^* of around (416 ± 110) ps, while from the analysis of the LZSM interference oscillations we extract an average decoherence time of around (483 ± 24) ps. These time scales are en par with those reported for advanced GaAs QDs^{41,42} which is a first indicator for low charge noise and an important quality measure for the van-der-Waals interfaces in the BLG-based heterostructure.

Results

The device used to form a DQD consists of a BLG flake encapsulated between two crystals of hBN placed on a global graphite back gate (BG), with two layers of metallic top gates (i.e., the split and finger gate layer) separated by aluminium oxide. Figure 1a shows a false-color scanning electron microscopy image of the gate structure of the device (see Methods for details)⁴³. The BG and split gates (SGs) are used to form a p-type channel connecting source and drain reservoirs. The potential along the channel can be controlled using a set of finger gates (FGs). A DQD is formed by locally overcompensating the potential set by the BG using two adjacent FGs, as schematically depicted in Fig. 1b (see also yellow FGs in Fig. 1a). Figure 1c shows a charge stability diagram of the DQD in the few electron regime. When increasing the FG voltages, especially on the right FG, V_R , the current through the DQD increases and the co-tunneling lines become more pronounced. This indicates that the interdot tunnel coupling can be sensitively tuned by the voltages applied to the FGs⁴⁴.

The first step towards studying quantum phase coherence in the DQD is to create an effective TLS and to characterize its energy dispersion using PAT spectroscopy. We focus on a single pair of triple

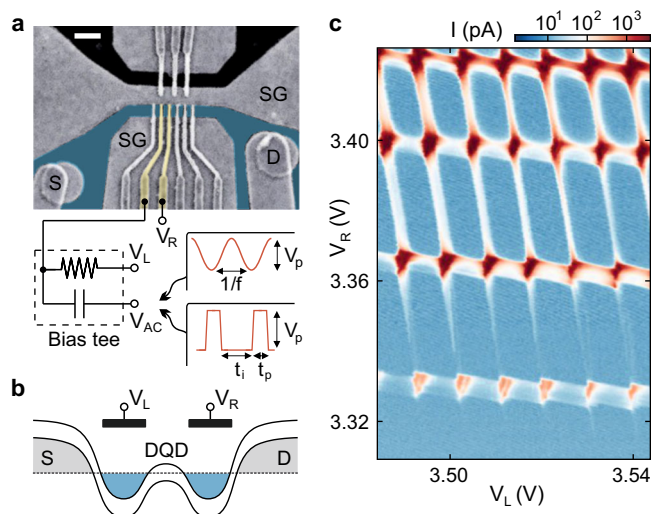


Fig. 1 | Bilayer graphene double quantum dot. **a** False-color scanning electron microscopy image of the DQD device. The scale bar measures 500 nm. The split gates (SG) together with the back gate (not shown) are used to define a narrow conductive channel connecting the source (S) and drain (D) reservoirs (highlighted in blue). The channel is crossed by finger gates (see yellow structures) used to locally tune the band edges to form QDs. Our so-called finger gate left is connected to a bias tee which allow applying DC (V_L) and AC voltages (V_{AC}). The voltage V_R is applied to the right finger gate. **b** Schematic of the conduction and valence band edge profile of the DQD highlighting the left and right finger gate, where V_L and V_R can be applied. **c** Charge stability diagram of the DQD at low electron occupation measured at a source-drain bias voltage of $V_{SD} = 0.5$ mV.

points, where a TLS is formed by a single excess electron that can be located either in the left or the right QD (see Fig. 2a) with the two states $|R\rangle := (N, M+1)$ and $|L\rangle := (N+1, M)$, where N and M is the electron occupation of the left (L) and the right (R) QD, respectively. For large detuning energies, ε , compared to the interdot tunnel coupling energy, $\Delta/2$, the eigenenergies of the TLS are given by $E_L = \varepsilon/2$ and $E_R = -\varepsilon/2$, where ε is the detuning energy between the two QDs (see white arrow in Fig. 2a and gray dashed lines in Fig. 2b). This approximation becomes invalid for $|\varepsilon| \lesssim \Delta$, where the eigenenergies are given by the more general form $E_{\pm} = \pm \frac{1}{2} \sqrt{\varepsilon^2 + \Delta^2}$ (see solid lines in Fig. 2b). The state of such a TLS can be represented on the Bloch sphere shown in Fig. 2c, using the states $|R\rangle$ and $|L\rangle$ as a basis.

PAT spectroscopy allows to map out the energy dispersion of the TLS and thereby to determine the tunnel coupling, which together with the detuning fully characterizes the system. This method relies on microwave excitation of electrons across the interdot tunnel barrier, which becomes possible whenever the microwave excitation is in resonance with the energy splitting of the QD states, i.e., $hf = E_+ - E_-$ with the microwave frequency f and Planck's constant h ^{41,45-47}. At a small bias voltage, we detune the energy levels of the QDs such that transport is blocked. An electron in the low energy state (see inset in Fig. 2h) can then only transfer into the higher state if the system absorbs a resonant microwave photon. The excited electron then can tunnel to the reservoir, contributing to a current through the device whose direction depends on the sign of the detuning energy.

Figure 2d shows a charge stability diagram of the triple point in Fig. 2a, recorded at zero bias voltage while applying a microwave excitation of $f = 9$ GHz to the left gate. Two parallel current resonances of opposite sign appear symmetrically around zero detuning. In order to map the energy splitting as a function of detuning, the microwave excitation frequency is varied. In the PAT measurements, also excited states could play a role, if energetically accessible⁴⁷. The absence of these excited states can be explained by the out-of-plane magnetic field of 1.8 T applied to the device, which polarizes the valley states (valley splitting of ≈ 1.5 meV) and also partly the spin states (spin splitting of ≈ 210 μ eV). The resonances split further with increasing frequency, as shown for $f = 15$ GHz and $f = 25$ GHz in Fig. 2e, f, respectively (see Supplementary Fig. 2 for more data). For a quantitative analysis, we measure the splitting of the PAT resonances along the V_L axis, δV_L , as a function of the applied microwave frequency, see line cut in Fig. 2g. At $\delta V_L < 0.2$ mV, the PAT resonances begin to overlap, setting a lower bound to the frequency range that can be investigated. The relation of δV_L and f is determined by the resonance condition ($hf = E_+ - E_-$) and can be expressed as

$$f(\delta V_L) = \frac{1}{h} \sqrt{(\alpha \delta V_L)^2 + \Delta^2}, \quad (1)$$

where α is the lever arm that converts the V_L axis to a detuning energy. We fit Eq. (1) to the data with the fit parameters α and Δ (see red line in Fig. 2h). This yields a tunnel coupling of $\Delta/(2h) = 2.1 \pm 0.2$ GHz and $\alpha = 194.5 \pm 1.1$ μ eV/mV, which is in good agreement with the lever arm obtained from DC finite bias spectroscopy measurements (see Supplementary Fig. 1). Additionally, similar measurements were conducted for a set of two different FG voltages ($V_L = 3.475$ V, $V_R = 3.38$ V, and $V_L = 3.555$ V, $V_R = 3.36$ V), which yield $\Delta/2h \approx 1.54$ GHz and $\Delta/2h \approx 7.87$ GHz, respectively. For the following measurements the regime of intermediate tunnel coupling (2.1 GHz) was chosen.

Besides studying the dispersion of the TLS, PAT spectroscopy measurements also probe its coherent properties. From the full width at half maximum, γ , of the PAT resonance, the ensemble decoherence time $T_{2,PAT}^* = 2h/(\alpha\gamma)$ of the charge degree of freedom can be estimated^{41,42,48}. The fits in Fig. 2g, yield a $T_{2,PAT}^*$ at the positive (red) and negative (blue) PAT peak of 422 ps and 291 ps, respectively. We assign the timescale extracted in this experiment to the ensemble

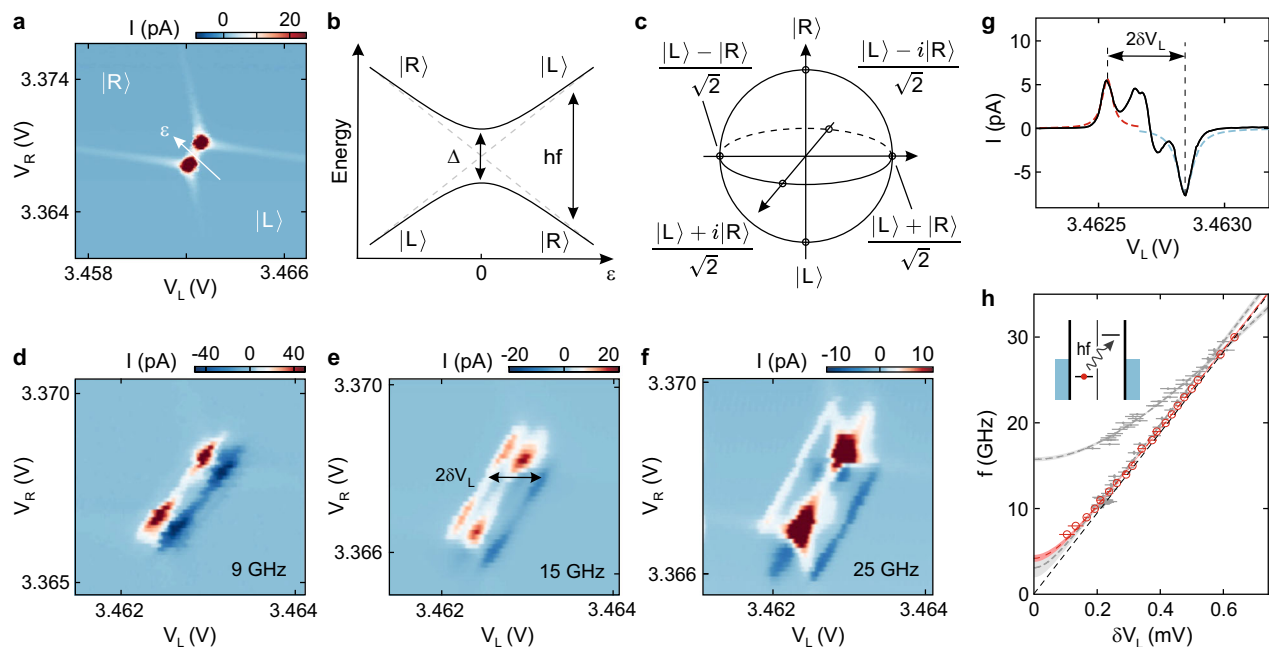


Fig. 2 | Photon-assisted tunneling. **a** Charge stability diagram of a pair of triple points at $V_{SD} = 50 \mu\text{V}$. The charge ground states $|R\rangle$ and $|L\rangle$, corresponding to the position of an excess electron in the DQD (left or right) and the axis of the detuning energy, ε , are indicated. **b** Energy diagram of the TLS. The energies of the uncoupled charge states $|R\rangle$ and $|L\rangle$ are shown by dashed gray lines. For non-zero tunnel coupling, $\Delta \neq 0$, a pair of hybridized eigenstates emerges with eigenenergies represented by the solid black lines, showing a splitting of Δ at zero detuning. The resonance condition required for PAT is given by $hf = \sqrt{\varepsilon^2 + \Delta^2}$. **c** Bloch sphere representation of the TLS with the charge states $|R\rangle$ and $|L\rangle$ on the poles. **d** Charge stability diagram of the triple point shown in **(a)** while applying a microwave excitation of $f = 9 \text{ GHz}$ and -36 dBm to the left FG. **e, f** Measurements as in **(d)** for $f = 15 \text{ GHz}$ and $f = 25 \text{ GHz}$, respectively. More data sets for different frequencies are presented in

Supplementary Fig. 2. The separation of the peaks, $2\delta V_L$, is measured to investigate the energy splitting of the TLS. **g** Cut through panel **e** along V_L . Lorentzians are fitted to the negative (blue) and positive (red) PAT peak. The arrow indicates where $2\delta V_L$ is extracted (see Supplementary Fig. 3 for more data). **h** Resonant excitation frequency as a function of δV_L (see **e**). The dashed red curve shows a fit according to $hf = \sqrt{(\alpha\delta V_L)^2 + \Delta^2}$ while the shaded bands mark the $\pm 1\sigma$ confidence interval. The dashed black line is a straight line through the origin with the slope of the lever arm $\alpha = 194.5 \mu\text{eV/mV}$. The gray data points in the background are the results for two distinct sets of FG voltages ($V_L = 3.475 \text{ V}$, $V_R = 3.38 \text{ V}$, $\Delta/2h \approx 1.54 \text{ GHz}$ and $V_L = 3.555 \text{ V}$, $V_R = 3.36 \text{ V}$, $\Delta/2h \approx 7.87 \text{ GHz}$). Inset: Schematic representation of the electrochemical potentials in a DQD illustrating the process of PAT.

decoherence time as it results from a current that is integrated over many pulse cycles and can thus be viewed as a time-ensemble average.

In order to obtain a better understanding of the dynamics of the TLS and to gain insight into the charge decoherence time, we perform LZSM interferometry measurements, a powerful technique, where the TLS is driven non-adiabatically through the anti-crossing of the energy levels. To this end, a voltage pulse with a finite rise time, $t_r \approx 140 \text{ ps}$, is applied to the left finger gate, see Fig. 3a. We initialize (i) the excess electron in the right QD by allowing it to relax into the ground state, $|R\rangle$, at a detuning $\varepsilon_i < 0$ for a time $t_i \approx 3 \text{ ns}$. To ensure a sufficient initialization but still keep a high signal-to-noise ratio, the initialization time was chosen such that $t_i \geq 1/\Gamma_{\text{comb}} \approx 1.6 \text{ ns}$, where Γ_{comb} is the combined tunneling rate through the DQD, estimated from finite bias spectroscopy (see Supplementary Fig. 1). The initial state of the TLS is shown in the level scheme (Fig. 3b (1)) as well as in the energy diagram and Bloch sphere representation (Fig. 3c (1)). After the initialization, the chemical potential of the left QD is shifted by a voltage pulse of nominal amplitude V_p , corresponding to an effective detuning pulse of amplitude A_p applied to the sample (see Methods for details). The change in detuning is approximated to occur at a constant rate $\nu = |\partial\varepsilon/\partial t| \approx 1.6 \mu\text{eV/ps}$. When passing the anti-crossing at zero detuning, the system undergoes a Landau-Zener (LZ) transition from the ground to the excited state with a transition probability given by⁴⁹

$$P_{LZ} = \exp\left(-\frac{\pi\Delta^2}{2\hbar\nu}\right), \quad (2)$$

and picks up a relative Stokes phase φ_S , marked in blue on the equator of the Bloch sphere in Fig. 3c (2). The LZ transition results in a superposition state with weights $1 - P_{LZ}$ and P_{LZ} in the ground and excited state, respectively (Fig. 3b (2), c (2)). The ratio of the weights is experimentally accessible via ν . In the adiabatic limit ($\hbar\nu \ll \Delta^2$), the system remains in the ground state, while in the non-adiabatic limit ($\hbar\nu \gg \Delta^2$), the entire wave function transitions to the excited state. After the first LZ transition, the system is allowed to time-evolve freely at the point of maximum detuning $\varepsilon_i + A_p$ for a time t_p (Fig. 3b (3), c (3)). It accumulates another phase contribution given by⁴⁹

$$\varphi_{ev} = \frac{1}{2\hbar} \int_{t_{LZ1}}^{t_{LZ2}} \sqrt{\varepsilon(t)^2 + \Delta^2} dt, \quad (3)$$

where t_{LZ1} is the time of the first (second) LZ transition (see gray shaded areas in Fig. 3a, c (3)). While the system is then returned to ε_i at “rate” ν , it undergoes a second LZ transition at zero detuning (Fig. 3b (4), c (4)), adding another phase contribution of φ_S . Both parts of the wave function interfere coherently, such that the final excitation probability is a function of the total relative phase $\varphi = \varphi_{ev} + 2\varphi_S$. Constructive (destructive) interference into the excited (ground) state occurs for $\varphi = 2n\pi$ ($\varphi = (2n+1)\pi$), $n \in \mathbb{N}_0$ ¹³. At the end of the pulse cycle, a projective readout of the final state is performed. An electron in the excited state $|L\rangle$ can tunnel out of the DQD and contribute to a current that is averaged over many pulse cycles, while an electron in the ground state $|R\rangle$ cannot leave the DQD (Fig. 3b(5)). In the Bloch sphere representation, the readout corresponds to a projection on the z axis (Fig. 3c (5)).

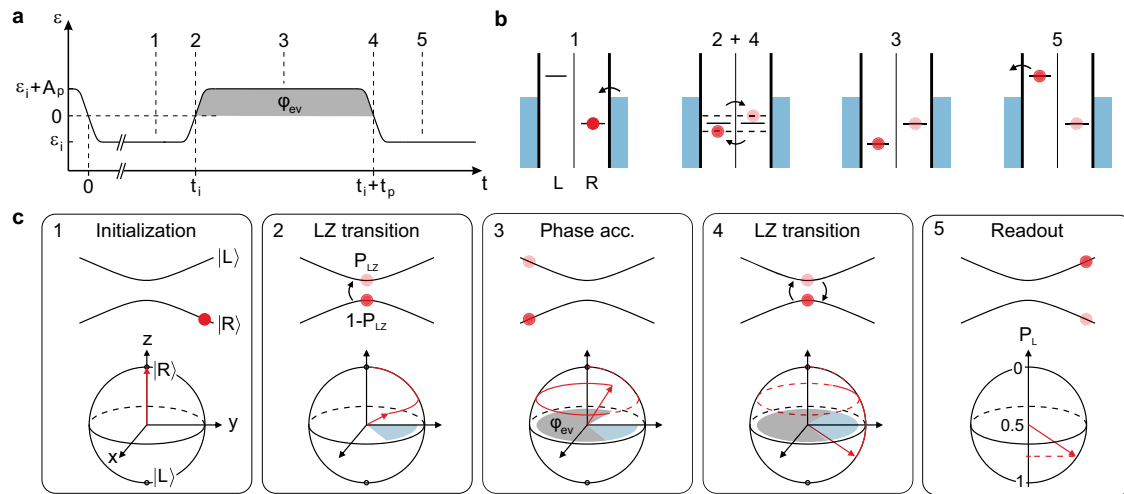


Fig. 3 | Pulse scheme and state manipulation in a LZSM interference experiment. **a** Time-dependent detuning driven by a voltage pulse applied to the left FG characterized by pulse amplitude, A_p , and durations t_p and t_i . **b** Schematics of the energy levels in the DQD while the pulse scheme in **(a)** is applied. **c** Time evolution of the TLS under the influence of the pulse scheme, shown in the energy diagram and on the Bloch sphere. (1) First, the system is initialized at ε_i for the duration of t_i (see **a**). An electron tunnels to the right QD (see **b**) and the system is in the ground state $|R\rangle$, as shown by the red dot and the red arrow. (2) The system is detuned to $\varepsilon_i + A_p$. The process is adiabatic except at the point of $\varepsilon = 0$ (see **a, b**), where a LZ transition into the excited state is possible. This creates a superposition state, depicted by two dots in the energy diagram, and a rotation of the Bloch vector

about the x axis. In this process, a relative Stokes phase φ_S is picked up, represented by the blue shaded area in the equator plane of the Bloch sphere. (3) During t_p , both components of the wave function evolve separately in time at a detuning $\varepsilon_i + A_p$, accumulating a relative phase φ_{ev} represented by the area shaded in gray. (4) When crossing $\varepsilon = 0$ again (see also panels **a, b**), a second LZ transition takes place and the initially separated wave functions interfere. (5) In the readout configuration, the detuning is set to ε_i again (see **a**). An electron in the excited state $|L\rangle$ can tunnel to the drain and contribute to the measured current, while an electron in the ground state would be trapped due to Coulomb blockade (see **b**). By this method the occupation probability of the excited state, P_L , is determined.

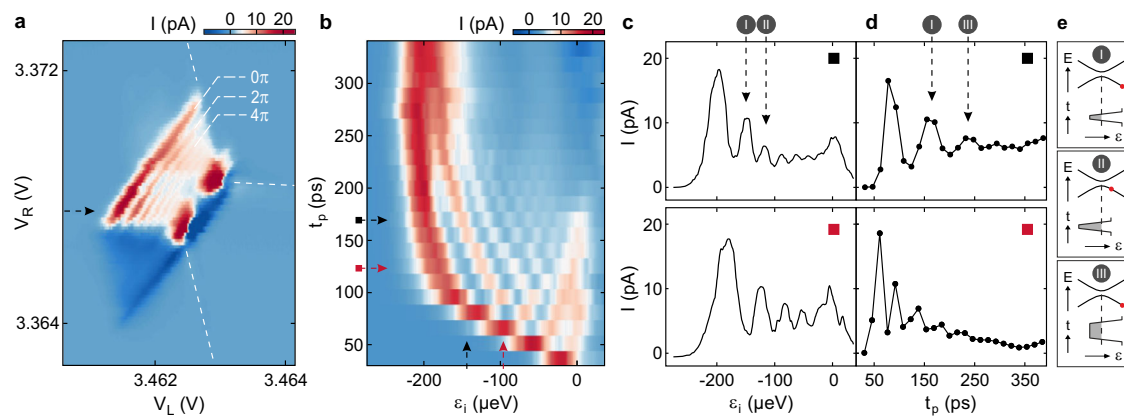


Fig. 4 | Coherent charge oscillations in the time domain. **a** Charge stability diagram of the triple point as in Fig. 2a, while a pulse of duration $t_p = 165$ ps and amplitude $A_p = 228$ μeV is applied to the DQD by the left FG. The black dashed lines highlight the co-tunneling lines. Fringes of increased current indicate coherent charge oscillations. Complementary data sets for different t_p and A_p are presented in Supplementary Fig. 4. **b** Oscillations in the time domain, obtained along the line cut indicated by the black arrow in **(a)**. Complementary data sets for different pulse

A_p are presented in Supplementary Fig. 5. **c** Cut along the detuning axis as indicated by the horizontal black and red arrows in **(b)**. Up to six interference maxima with decreasing intensity can be distinguished. **d** Cut along the t_p axis as indicated by the vertical black and red arrows in **(b)**. **e** Schematics illustrating the configurations at the maxima labeled (I)–(III) in **(c, d)** indicating the influence of the parameters ε_i and t_p on the relative phase φ_{ev} .

Figure 4a shows a charge stability diagram of the transition between $|L\rangle = (N+1, M)$ and $|R\rangle = (N, M+1)$ while applying a voltage pulse to the left FG (V_L) as described above. Parallel to the zero detuning line of the triple point, a series of additional lines of increased current can be observed, that are constrained by the co-tunneling lines and the pulse amplitude. This is a clear signature of coherent charge oscillations of one excess electron, where the fringes indicate constructive interference. The first and strongest fringe corresponds to the situation where the pulse just reaches zero detuning, i.e., $\varepsilon_i + A_p = 0$ during the time span t_p , and the electron can first tunnel over into the

other QD. At every following line, the relative phase has increased by another 2π . The region of negative current in Fig. 4a can be attributed to charge pumping occurring outside of the gate configurations where the measurement scheme presented in Fig. 3a operates. We find the data in agreement with the adiabatic-impulse approximation⁴⁹ as no interference signature is visible before reaching the first fringe.

The loss of charge coherence over time can be explored by performing LZSM interferometry in the time domain, i.e., as a function of the pulse duration t_p and detuning energy during initialization ε_i , as shown in Fig. 4b. An effective pulse amplitude of $A_p \approx 228$ μeV can be

deduced from the position of the first interference fringe at $t_p \approx 200$ ps, which yields a rate of $v \approx 1.6$ $\mu\text{eV}/\text{ps}$. Oscillations appear along the detuning and time axes. This observation can be explained by considering how both parameters influence the accumulated phase. Figure 4c plots line cuts along the detuning axis in the time domain (see horizontal dashed lines in Fig. 4b). Up to six interference maxima can be identified before the signal is overlaid by the broad feature at $\varepsilon_i = 0$, which originates from the tunneling of charge carriers through the DQD when the electrochemical potential in the left QD is aligned with the bias during the initialization step. In Fig. 4c, two oscillation maxima are highlighted by (I) and (II) and the acquired phase is indicated by the gray area in the corresponding schematics shown in Fig. 4e. Maximum (I) corresponds to the configuration where a relative phase of 2π is acquired during one pulse cycle. Following the detuning axis to the next maximum (II), the phase increases by another 2π as the system is taken further beyond zero detuning, leading to a higher maximum value of the integrand in Eq. (3) (compare gray areas in schematics (I) and (II)). The absence of oscillations on the first fringe ($\varepsilon_i \approx -200$ μeV) in Fig. 4a can be attributed to the distortion of the pulse when transmitted through the setup, as has been studied in GaAs/AlGaAs DQDs¹⁶. Fig. 4d shows line cuts along the time axis (see vertical dashed lines in Fig. 4b), which show oscillations that are damped due to the loss of quantum phase coherence. However, the resolution along the time axis is not sufficient for a quantitative

decoherence analysis. The expected oscillation period is given by $T = h/\sqrt{\varepsilon^2 + \Delta^2}$ ⁴⁰. Going from maximum (I) to (III) also adds a phase of 2π , in this case by prolonging t_p and thus expanding the integration bounds in Eq. (3) (compare gray areas in schematics (I) and (III) in Fig. 4e).

Next, we focus on the amplitude domain to quantitatively analyze the loss of phase coherence^{9,13,50–52}. The pulse amplitude A_p is another experimental knob to tune the relative phase of the TLS superposition state. Figure 5a shows the current through the device in a pulsed measurement of constant $t_p = 200$ ps, as a function of ε_i and A_p . The data show several parallel interference fringes with decreasing intensity. The first and most prominent fringe, labeled (0), corresponds to the situation sketched in the upper schematic in Fig. 5b, where the pulse takes the system to zero detuning during t_p . At the second fringe, labeled (I), A_p has increased such that the pulse crosses zero detuning and a relative phase of 2π is accumulated, see lower schematic in Fig. 5b. The intensity along a single fringe shows no periodic modulation, which confirms that quantum coherence is only lost between two pulses^{6,49}. In the case of multiple coherent LZ transitions, the intensity along a given fringe would additionally be modulated due to the interference of more than two consecutive LZ transitions, whereas only a featureless current would be expected if decoherence occurred between all LZ transitions, i.e., faster than the pulse duration. Hence, the pulse duration ($t_p = 200$ ps) and the initialization time (here:

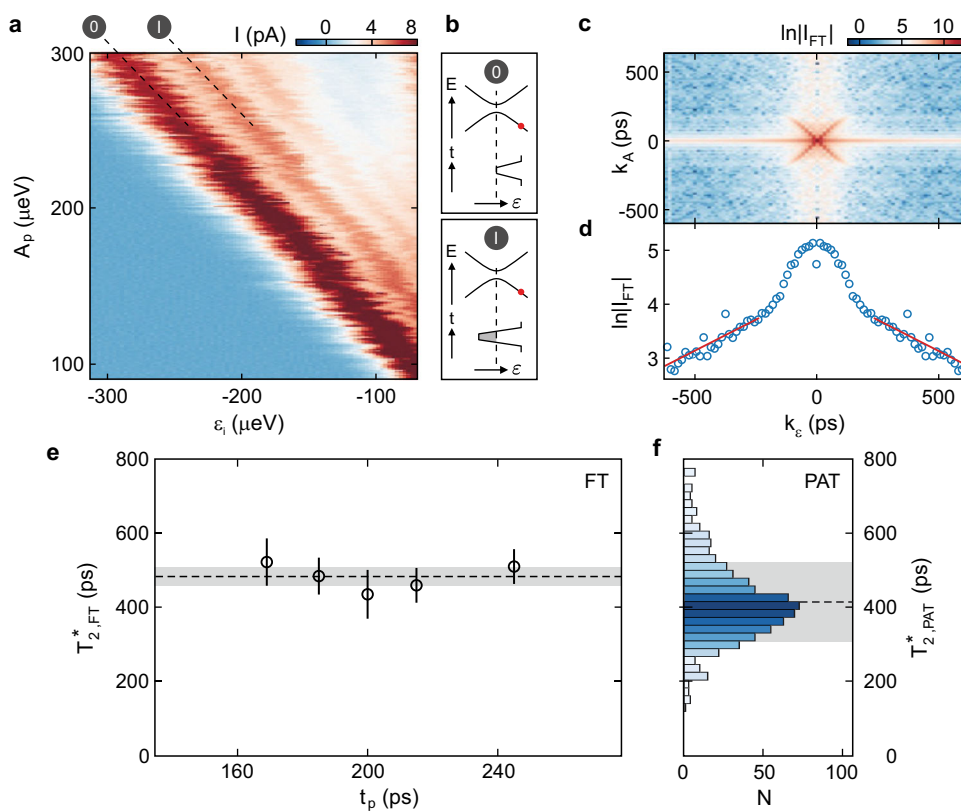


Fig. 5 | Coherent oscillations in the amplitude domain. **a** Current through the device as a function of the initialization detuning ε_i and pulse amplitude A_p , at a constant duration of $t_p = 200$ ps. LZSM interference fringes of two consecutive passages through zero detuning can be seen. Complementary data sets are shown in Supplementary Figs. 6 and 7. **b** Schematics illustrating the pulse and energy diagram on the points (0) and (I) in (a). The red dot illustrates the readout/initialization configuration. **c** Fourier transform (FT) of the data in (a). The crossing in the center is attributed to the time dependence of the phase⁵⁰, while the decreasing background contains information on the decoherence in detuning-space. **d** Line cut along the k_ε axis averaged over a small area in (c). The peak around $k_\varepsilon = 0$ is attributed to low-frequency noise. Red lines are fits to Eq. (5). **e** Decoherence time

$T_{2,FT}^*$ obtained from measurements as in panel a at different pulse widths t_p , revealing an average of $T_{2,FT}^* = (483 \pm 24)$ ps (dashed line and gray shaded area). **f** Histogram of $T_{2,PAT}^*$ extracted from the FWHM, γ , of Lorentzian line shapes fit to the PAT peaks as illustrated in Fig. 2g. $T_{2,PAT}^*$ is calculated according to $T_{2,PAT}^* = 2h/(\alpha\gamma)$ ^{41, 42, 48}. The histogram contains data points from 18 different data sets measured in a frequency range from $f = 9$ to 30 GHz. For each frequency, PAT peaks at different V_R have been evaluated. A total of 729 data points for $T_{2,PAT}^*$ are shown in the histogram, where N denotes the number of points in one bin. The average measures $T_{2,PAT}^* = (416 \pm 110)$ ps, highlighted by the dashed black line and the gray shaded area.

$t_i = 3$ ns) give a lower and upper bound for the timescale of decoherence.

In order to quantify the decoherence time, we consider the Fourier transform (FT) of the current signal,

$$I_{\text{FT}}(k_\varepsilon, k_A) = \iint \exp(-ik_\varepsilon \varepsilon - ik_A A_p) I(\varepsilon, A_p) d\varepsilon dA_p. \quad (4)$$

The relevant timescale can be obtained from the decay of the Fourier amplitude^{13,50,52},

$$\ln|I_{\text{FT}}(k_\varepsilon, k_A)| = a - k_\varepsilon / T_{2,\text{FT}}^*, \quad (5)$$

where a is an unknown proportionality factor and $T_{2,\text{FT}}^*$ is the ensemble decoherence time extracted by this experiment. Figure 5c shows the Fourier transform of the symmetrized current signal (with respect to A_p) from Fig. 5a. The prominent cross-like feature contains information on the time between subsequent crossings of zero detuning and the phase accumulated in between⁵⁰, but is of no further relevance for the determination of $T_{2,\text{FT}}^*$. To obtain $T_{2,\text{FT}}^*$, we follow refs. 50–52 and analyze the decay of $\ln(I_{\text{FT}})$ as a function of k_ε . Figure 5d shows the average of 100 line cuts through the data in Fig. 5c along k_ε , that do not include the cross-like feature. Similar to other works, the central peak is likely caused by low-frequency noise and therefore not considered in the following^{13,51,52}. The red solid lines represent the best fit to Eq. (5) resulting in $T_{2,\text{FT}}^* = (435 \pm 66)$ ps. Figure 5e shows $T_{2,\text{FT}}^*$ extracted from measurements as in Fig. 5a, c, d for different pulse widths t_p . The results yield an average value of $T_{2,\text{FT}}^* = (483 \pm 24)$ ps (see dashed line and gray shaded area in Fig. 5e) with an additional systematic uncertainty of ≈ 70 ps that stems from the uncertainty in determining the lever arm.

Discussion

For comparison, Fig. 5f shows a histogram of $T_{2,\text{PAT}}^*$ extracted from fits to PAT peaks as shown exemplary in Fig. 2g, measured at different excitation frequencies in a range of $f = 9$ to 30 GHz (see also Supplementary Figs. 2 and 3). Evaluating a total of 729 data points, we find a distribution around an average $T_{2,\text{PAT}}^* = (416 \pm 110)$ ps (see dashed line and gray shaded area in Fig. 5f), which is slightly smaller than the average $T_{2,\text{FT}}^*$ obtained from LZSM interferometry. The significant variation of $T_{2,\text{PAT}}^*$, evident from the large error and distribution in Fig. 5f, is likely attributed to slight fluctuations in the power of the applied pulse caused by the frequency-dependent transmission through the setup. The discrepancy between $T_{2,\text{PAT}}^*$ and $T_{2,\text{FT}}^*$ can be explained by charge fluctuations, which are slower than the coherence time but faster than the integration time of the measurement, and thus may result in a statistical broadening of the PAT resonances. Furthermore, the applied microwave excitation causes a power broadening of the PAT resonances. Both effects lead to an underestimation of $T_{2,\text{PAT}}^*$, which therefore only serves as a lower bound. Interestingly, our findings are comparable to the longest decoherence times determined by PAT, $T_{2,\text{PAT}}^*$, reported in GaAs (400 ps⁴¹, 250 ps⁴²) and are larger than those reported for carbon nanotubes (280 ps⁴⁶), whereas reported $T_{2,\text{FT}}^*$ determined by LZSM interference measurements ranges from 100 ps in a Si DQD⁵² to 4 ns in a GaAs DQD¹³. When comparing these values with our results, it is important to note that the ensemble decoherence time T_2^* is sensitive to noise contributions from a broad frequency spectrum and depends on the exact measurement configuration. In semiconductor materials, the dominant contributions are intrinsic noise originating from charge fluctuations in the material, as well as charge noise coupling in via the gates⁴⁰, where low-frequency noise is assumed to be dominant, typically approximated with an $1/f$ spectral density^{42,53–56}. Note that charge noise can affect both Δ and ε , whereas the latter effect is dominant due to the stronger dependence of ε on the gate voltages. In first approximation, charge noise couples

in proportionally to the slope of the energy bands, $|dE_\pm/d\varepsilon|$. This leads to an increasing decoherence time when moving closer to the sweet spot $\varepsilon = 0$ where $|dE_\pm/d\varepsilon|$ vanishes^{40,42}. In LZSM interferometry, such as in our experiment, the TLS evolves at finite detuning, $\varepsilon \neq 0$, hence $T_{2,\text{FT}}^*$ just serves as a lower bound. In particular, the implementation of a charge sensor will allow the direct measurement of coherent charge oscillations (e.g., in a Ramsey experiment) at the sweet spot where the influence of charge noise is further reduced to a minimum promising longer decoherence times⁵⁶. Moreover, in further experiments, including charge echo measurements, the spectral distribution of charge noise in BLG DQDs could be investigated. These techniques have the potential to cancel out the effect of quasi-static noise and increase the charge decoherence time^{57,58}. Furthermore, temperature-dependent decoherence measurements allow to quantify electron-phonon coupling, an intrinsic source of decoherence in QDs, as demonstrated in GaAs QDs⁴⁰. Charge coherence experiments can also be extended to DQDs in other 2D materials such as WSe₂ and MoSe₂³⁵. The high sensitivity of this type of experiment can be exploited to characterize material-dependent properties such as defect-induced and interfacial charge noise and electron-phonon coupling, which are expected to be different from BLG.

In summary, we have shown coherent charge oscillations in a BLG DQD, which we discuss in the framework of Landau-Zener-Stückelberg interference. Our findings constitute the first observation of phase coherent oscillations in a graphene QD device and underline this material's potential in the field of quantum technology. We compare the ensemble decoherence times, determined independently from a Fourier analysis of coherent oscillations in the amplitude domain and from PAT spectroscopy. Both methods consistently yield average decoherence times T_2^* in the range of 400–500 ps.

Methods

The device was fabricated from a BLG flake encapsulated between two hBN crystals of approximately 25 nm (top) and 45 nm (bottom) thicknesses using conventional van-der-Waals stacking techniques. A graphite flake is used as a back gate (BG). The source and drain are etched through the top hBN to contact the BLG using reactive ion etching. The 30 nm thick Cr/Au split gates (SGs) with a lateral separation of 80 nm are deposited on top of the heterostructure. Isolated from the SGs by 15 nm thick atomic layer deposited (ALD) Al₂O₃, we fabricate 70 nm wide and 75 nm thick Cr/Au finger gates (FGs) with a pitch of 150 nm. Figure 1a shows a false color scanning electron micrograph of the gate pattern.

In order to perform high frequency gate manipulation, the sample is mounted on a custom-made printed circuit board (PCB). The DC lines are low-pass-filtered (10 nF capacitors to ground). All FGs are connected to on-board bias-tees, allowing for AC and DC control on the same gate (see Fig. 1a). Microwaves are generated by an Agilent E8257D microwave source and pulse sequences are generated by a Keysight M8195A arbitrary waveform generator with a sampling rate of 65 GS/s. The AC signals are attenuated by -10 dB at room temperature and further by -26 dB in the cryostat. The nominal pulse amplitude V_p output by the instruments is converted into an effective amplitude A_p applied to the sample by measuring a charge transition as a function of ε and V_p . This calibration converts the voltage V_p into an energy and takes into account losses due to attenuators, cables and the PCB. For a pulse width t_p exceeding the finite rise time of $t_r \approx 140$ ps, we determine a ratio of $A_p/V_p = 1.50 \pm 0.02$ $\mu\text{eV}/\text{mV}$ which is significantly reduced for $t_p < t_r$.

All measurements are performed in a ³He/⁴He dilution refrigerator at a base temperature of around 15 mK and at an electron temperature of around 60 mK using standard DC measurement techniques. The current through the device is amplified and converted into a voltage with a home-built I–V converter at a gain of 10⁸. A p-type channel between source and drain is defined by applying voltages of -3.5 V to

the BG as well as 1.82 V and 1.825 V to the outer and middle SGs, respectively. Positive voltages applied to the left and right FGs, V_L and V_R , form a DQD (see Fig. 1b). An out-of-plane magnetic field of 1.8 T has been applied to adjust the tunneling rates.

Data availability

The data used in this study are available in a Zenodo repository under accession code <https://doi.org/10.5281/zenodo.10091584>.

References

- Landau, L. D. Zur theorie der energieubertragung ii. *Phys. Sov. Union* **2**, 46–51 (1932).
- Zener, C. Non-adiabatic crossing of energy levels. *Proc. R. Soc. London A* **137**, 696–702 (1932).
- Stückelberg, E. Theorie der unelastischen stöße zwischen atomen. *Helv. Phys. Acta* **5**, 369–423 (1932).
- Majorana, E. Atomi orientati in campo magnetico variabile. *Il Nuovo Cimento* **9**, 43–50 (1932).
- Ivakhnenko, O., Shevchenko, S. & Nori, F. Nonadiabatic Landau–Zener–Stückelberg–Majorana transitions, dynamics, and interference. *Phys. Rep.* **995**, 1–89 (2023).
- Dupont-Ferrier, E. et al. Coherent coupling of two dopants in a silicon nanowire probed by Landau-Zener-Stückelberg interferometry. *Phys. Rev. Lett.* **110**, 136802 (2013).
- Childress, L. & McIntyre, J. Multifrequency spin resonance in diamond. *Phys. Rev. A* **82**, 033839 (2010).
- Fuchs, G. D., Burkard, G., Klimov, P. V. & Awschalom, D. D. A quantum memory intrinsic to single nitrogen–vacancy centres in diamond. *Nat. Phys.* **7**, 789–793 (2011).
- Berns, D. et al. Amplitude spectroscopy of a solid-state artificial atom. *Nature* **455**, 51–57 (2008).
- Petta, J. R., Lu, H. & Gossard, A. C. A coherent beam splitter for electronic spin states. *Science* **327**, 669–672 (2010).
- Gaudreau, L. et al. Coherent control of three-spin states in a triple quantum dot. *Nat. Phys.* **8**, 54–58 (2012).
- Stehlik, J. et al. Landau-Zener-Stückelberg interferometry of a single electron charge qubit. *Phys. Rev. B* **86**, 121303 (2012).
- Cao, G. et al. Ultrafast universal quantum control of a quantum-dot charge qubit using Landau–Zener–Stückelberg interference. *Nat. Commun.* **4**, 1401 (2013).
- Dovzhenko, Y. et al. Nonadiabatic quantum control of a semiconductor charge qubit. *Phys. Rev. B* **84**, 161302 (2011).
- Wang, L., Tu, T., Gong, B., Zhou, C. & Guo, G.-C. Experimental realization of non-adiabatic universal quantum gates using geometric Landau-Zener-Stückelberg interferometry. *Sci. Rep.* **6**, 1–7 (2016).
- Ota, T., Hitachi, K. & Muraki, K. Landau-Zener-Stückelberg interference in coherent charge oscillations of a one-electron double quantum dot. *Sci. Rep.* **8**, 1–8 (2018).
- Nalbach, P., Knörzer, J. & Ludwig, S. Nonequilibrium Landau-Zener-Stueckelberg spectroscopy in a double quantum dot. *Phys. Rev. B* **87**, 165425 (2013).
- Yoneda, J. et al. A quantum-dot spin qubit with coherence limited by charge noise and fidelity higher than 99.9%. *Nat. Nanotechnol.* **13**, 102–106 (2018).
- Zajac, D. M. et al. Resonantly driven CNOT gate for electron spins. *Science* **359**, 439–442 (2018).
- Philips, S. G. et al. Universal control of a six-qubit quantum processor in silicon. *Nature* **609**, 919–924 (2022).
- Hendrickx, N. W. et al. A four-qubit germanium quantum processor. *Nature* **591**, 580–585 (2021).
- Petta, J. R. et al. Coherent manipulation of coupled electron spins in semiconductor quantum dots. *Science* **309**, 2180–2184 (2005).
- Nowack, K. C. et al. Single-shot correlations and two-qubit gate of solid-state spins. *Science* **333**, 1269–1272 (2011).
- Trauzettel, B., Bulaev, D., Loss, D. & Burkard, G. Spin qubits in graphene quantum dots. *Nat. Phys.* **3**, 192–196 (2007).
- McCann, E. & Koshino, M. The electronic properties of bilayer graphene. *Rep. Prog. Phys.* **76**, 056503 (2013).
- Rozhkov, A. V., Sboychakov, A. O., Rakhmanov, A. L. & Nori, F. Electronic properties of graphene-based bilayer systems. *Phys. Rep.* **648**, 1–104 (2016).
- Icking, E. et al. Transport spectroscopy of ultraclean tunable band gaps in bilayer graphene. *Adv. Electron. Mater.* **8**, 2200510 (2022).
- Kurzmann, A. et al. Charge detection in gate-defined bilayer graphene quantum dots. *Nano Lett.* **19**, 5216–5221 (2019).
- Banszerus, L. et al. Dispersive sensing of charge states in a bilayer graphene quantum dot. *Appl. Phys. Lett.* **118**, 093104 (2021).
- Banszerus, L. et al. Spin-valley coupling in single-electron bilayer graphene quantum dots. *Nat. Commun.* **12**, 5250 (2021).
- Kurzmann, A. et al. Kondo effect and spin-orbit coupling in graphene quantum dots. *Nat. Commun.* **12**, 1–6 (2021).
- Tong, C. et al. Tunable valley splitting and bipolar operation in graphene quantum dots. *Nano Lett.* **21**, 1068–1073 (2021).
- Banszerus, L. et al. Spin relaxation in a single-electron graphene quantum dot. *Nat. Commun.* **13**, 3637 (2022).
- Gächter, L. et al. Single-shot spin readout in graphene quantum dots. *PRX Quantum* **3**, 020343 (2022).
- Zhang, Z.-Z. et al. Electrotunable artificial molecules based on van der Waals heterostructures. *Sci. Adv.* **3**, e1701699 (2017).
- Boddison-Chouinard, J. et al. Gate-controlled quantum dots in monolayer WSe₂. *Appl. Phys. Lett.* **119**, <https://doi.org/10.1063/5.0062838> (2021).
- Martins, F. et al. Noise suppression using symmetric exchange gates in spin qubits. *Phys. Rev. Lett.* **116**, 116801 (2016).
- Botzern, T. et al. Quadrupolar and anisotropy effects on dephasing in two-electron spin qubits in GaAs. *Nat. Commun.* **7**, 1–5 (2016).
- Ward, D. et al. State-conditional coherent charge qubit oscillations in a Si/SiGe quadruple quantum dot. *npj Quantum Inf.* **2**, 1–6 (2016).
- Hayashi, T., Fujisawa, T., Cheong, H. D., Jeong, Y. H. & Hirayama, Y. Coherent manipulation of electronic states in a double quantum dot. *Phys. Rev. Lett.* **91**, 226804 (2003).
- Petta, J. R., Johnson, A. C., Marcus, C. M., Hanson, M. P. & Gossard, A. C. Manipulation of a single charge in a double quantum dot. *Phys. Rev. Lett.* **93**, 186802 (2004).
- Petersson, K. D., Petta, J. R., Lu, H. & Gossard, A. C. Quantum coherence in a one-electron semiconductor charge qubit. *Phys. Rev. Lett.* **105**, 246804 (2010).
- Banszerus, L. et al. Electron-hole crossover in gate-controlled bilayer graphene quantum dots. *Nano Lett.* **20**, 7709–7715 (2020).
- Banszerus, L. et al. Single-electron double quantum dots in bilayer graphene. *Nano Lett.* **20**, 2005–2011 (2020).
- Oosterkamp, T. H. et al. Microwave spectroscopy of a quantum-dot molecule. *Nature* **395**, 873–876 (1998).
- Mavalankar, A. et al. Photon-assisted tunneling and charge dephasing in a carbon nanotube double quantum dot. *Phys. Rev. B* **93**, 235428 (2016).
- van Diepen, C. J. et al. Automated tuning of inter-dot tunnel coupling in double quantum dots. *Appl. Phys. Lett.* **113**, 033101 (2018).
- Abragam, A. *The Principles of Nuclear Magnetism: The International Series of Monographs on Physics* 32 (Oxford University Press, Oxford, 1983).
- Shevchenko, S. N., Ashhab, S. & Nori, F. Landau–Zener–Stückelberg interferometry. *Phys. Rep.* **492**, 1–30 (2010).
- Rudner, M. S. et al. Quantum phase tomography of a strongly driven qubit. *Phys. Rev. Lett.* **101**, 190502 (2008).
- Forster, F. et al. Characterization of qubit dephasing by Landau-Zener-Stückelberg-Majorana interferometry. *Phys. Rev. Lett.* **112**, 116803 (2014).

52. Gonzalez-Zalba, M. et al. Gate-sensing coherent charge oscillations in a silicon field-effect transistor. *Nano Lett.* **16**, 1614–1619 (2016).
53. Fujisawa, T. & Hirayama, Y. Charge noise analysis of an AlGaAs/GaAs quantum dot using transmission-type radio-frequency single-electron transistor technique. *Appl. Phys. Lett.* **77**, 543–545 (2000).
54. Buizert, C. et al. *InSitu* reduction of charge noise in GaAs/Al_xGa_{1-x}As Schottky-Gated Devices. *Phys. Rev. Lett.* **101**, 226603 (2008).
55. Connors, E., Nelson, J., Qiao, H., Edge, L. & Nichol, J. Low-frequency charge noise in Si/SiGe quantum dots. *Phys. Rev. B* **100**, 165305 (2019).
56. Kim, D. et al. Microwave-driven coherent operation of a semiconductor quantum dot charge qubit. *Nat. Nanotechnol.* **10**, 243–247 (2015).
57. Shi, Z. et al. Coherent quantum oscillations and echo measurements of a Si charge qubit. *Phys. Rev. B* **88**, 075416 (2013).
58. Wang, B.-C. et al. Coherent control and charge echo in a GaAs charge qubit. *Europhys. Lett.* **117**, 57006 (2017).
59. Albrecht, W., Moers, J. & Hermanns, B. HNF - Helmholtz Nano Facility. *J. Large-Scale Res. Facil.* **3**, 112 (2017).

Acknowledgements

The authors thank F. Hassler for fruitful discussions, F. Lentz, S. Trelenkamp, M. Otto and D. Neumaier for help with sample fabrication and S. Tautz and M. Ternes for providing access to the AWG Keysight M8195A. This project has received funding from the European Union's Horizon 2020 research and innovation program under grant agreement No. 881603 (Graphene Flagship) and from the European Research Council (ERC) under grant agreement No. 820254, the Deutsche Forschungsgemeinschaft (DFG, German Research Foundation) under Germany's Excellence Strategy - Cluster of Excellence Matter and Light for Quantum Computing (ML4Q) EXC 2004/1 - 390534769, through DFG (STA 1146/11-1), and by the Helmholtz Nano Facility⁵⁹. K.W. and T.T. acknowledge support from JSPS KAKENHI (Grant Numbers 19H05790, 20H00354 and 21H05233).

Author contributions

L.B., C.V. and C.S. designed the experiment. L.B., K.H., S.M. and E.I. fabricated the device. K.H., L.B., A.S. and A.P. performed the measurements and analyzed the data. K.W. and T.T. synthesized the hBN crystals. C.V. and C.S. supervised the project. K.H., L.B., A.S., C.V. and C.S. wrote

the manuscript with contributions from all authors. K.H. and L.B. contributed equally to this work.

Funding

Open Access funding enabled and organized by Projekt DEAL.

Competing interests

The authors declare no competing interests.

Additional information

Supplementary information The online version contains supplementary material available at <https://doi.org/10.1038/s41467-023-43541-3>.

Correspondence and requests for materials should be addressed to K. Hecker.

Peer review information *Nature Communications* thanks the anonymous reviewers for their contribution to the peer review of this work. A peer review file is available.

Reprints and permissions information is available at <http://www.nature.com/reprints>

Publisher's note Springer Nature remains neutral with regard to jurisdictional claims in published maps and institutional affiliations.

Open Access This article is licensed under a Creative Commons Attribution 4.0 International License, which permits use, sharing, adaptation, distribution and reproduction in any medium or format, as long as you give appropriate credit to the original author(s) and the source, provide a link to the Creative Commons licence, and indicate if changes were made. The images or other third party material in this article are included in the article's Creative Commons licence, unless indicated otherwise in a credit line to the material. If material is not included in the article's Creative Commons licence and your intended use is not permitted by statutory regulation or exceeds the permitted use, you will need to obtain permission directly from the copyright holder. To view a copy of this licence, visit <http://creativecommons.org/licenses/by/4.0/>.

© The Author(s) 2023